JSTQE-CON-ASEL2026-10328-2025.R1

Exploring High Efficiency PCSELs Using Probabilistic Markov Chain Model

Jingzhao Liu, Xingyu Zhao, Daehyun Kim, Jonathan R. Orchard, David T. D. Childs, Member, IEEE, Richard J. E. Taylor, Paul Harvey, Member, IEEE, Stephen J. Sweeney, Senior Member, IEEE and Richard A. Hogg

***Abstract* — In this work, device designs to improve the power conversion efficiency of PCSELs are analyzed by a probabilistic Markov chain model. Critical comparison of total parasitic loss, output ratio, threshold current and power conversion efficiency at 1 W are considered. This is carried out for a range of possible new device designs that address self-absorption in the boundary PC to the PCSEL active element.**

***Index Terms* — Photonic crystal, PCSEL, modelling, probabilistic Markov chain**

I. INTRODUCTION

Photonic crystal surface emitting lasers (PCSELs) are a new class of semiconductor lasers that boast both high brightness and high functionality while maintaining the merits of semiconductor lasers, making them of significant research interest. [1] The large stable modes of the PCSEL allow high single-mode powers [2-5], bringing the opportunity for new applications of laser diodes that bridge the brightness gap between solid-state laser systems and laser diodes. Whilst record brightness has been achieved, [3] power conversion efficiency (PCE) must be suitable for application roll out. [6-7]

Applying unpumped photonic crystal (PC) boundaries is a conventional route to enhance PCE. In our recent study, we explored the loss mechanism of PCSELs with this conventional structure. Introducing self-absorption loss due to the unpumped quantum well active element in the unpumped boundary region, we showed that in-plane loss ($\alpha_{//}$) and internal loss (α_i) of the PCSEL are interlinked. [8]

In this paper we extend this simulation to explore a range of device designs to minimize parasitic loss in PCSELs by removing this self-absorption. We begin by describing the device types to be explored, and reviewing the Probabilistic Markov chain (PMC) model. We then describe the inputs and outputs to the simulation. We then explore the effects of butt-coupled passive sections in the boundary PC region, selective area intermixing the active element in the boundary PC region and using a second contact to the boundary PC. The additional contact device renders the boundary transparent, whilst the other two approaches maintain an internal loss only.

Various characteristics of these techniques are explored and the PCE for an exemplary 1 W source are discussed. For the butt-coupled device we consider the fabrication related issues of scattering loss at the etched/regrown waveguide interface. For the selective area intermixed device, the lateral extent of the transition from active to passive wavelengths is also considered. We include additional waste power in the case of the dual contact device in terms of the calculation of PCE. A critical comparison of approaches is made, and possible future research avenues discussed.

II. DEVICE TYPES

Figure 1 shows a schematic of different designs of PCSEL devices and their respective spatial loss/gain conditions. It should be clarified that the schematic PC (dots) in Figure 1 are not to real scale, with the active element containing several hundreds of PC atoms on one side. The yellow dots schematics shown in Figure 1 represent the contact-covered PC atoms, that are in gain, and are lasing. It has been discussed in previous studies that the current spreading region is small compared to the leakage of photons into the surrounding PC boundary, so the transition between gain and loss is considered to be abrupt in this study. [8]

Figure 1(a) is PCSEL with an absorptive boundary (dark red dots), in which the PCs are not pumped and have self-absorption loss caused by the absorptive QWs in the PC boundary region. [8] The schematic graph indicates the loss/gain characteristics of the active element, where outside the contact, the propagating optical power is subject to self-absorption in the unpumped quantum wells. This device schematic represents current approaches to minimizing parasitic loss [4-7, 9-11]. The design has been analyzed, and the interconnection of in-plane loss and internal loss has been highlighted in previous studies [8]

Figures 1(b) and 1(c) consider widely utilized monolithic integration technologies to realize passive boundary PC elements. Figure 1(b) is a PCSEL utilizing butt-coupled waveguide technology. Here etching of the active element and epitaxial regrowth of a passive waveguide are employed to realize active and passive regions. This technology is a critical building block for large scale InP photonic integrated circuits.

This work is supported in part through EPSRC Project EP/X032868/1, "I-STEER". The manuscript is submitted for review on 20th November 2025. *(Corresponding author: Jingzhao Liu).*

Jingzhao Liu, Xingyu Zhao and Stephen J. Sweeney are with James Watt School of Science and Engineering, University of Glasgow, Glasgow, G12 8QQ, United Kingdom (e-mail: j.liu.8@research.gla.ac.uk , x.zhao.3@research.gla.ac.uk and stephen.j.sweeney@glasgow.ac.uk)

Daehyun Kim and Richard A. Hogg are with Aston Institute for Photonic Technologies, Aston University, Birmingham, B4 7ET, United Kingdom (e-mail: r.hogg1@aston.ac.uk and d.kim3@aston.ac.uk)

Jonathan R. Orchard and Richard J. E. Taylor are with Vector Photonics, Building 4.05 West of Scotland, Science Park Kelvin Campus, 2317 Maryhill Rd, Glasgow, G20 0SP, United Kingdom (e-mail jon.orchard@vectorphotonics.com and richard.taylor@vectorphotonics.com)

David T. D. Childs was formerly with the University of Glasgow, now with Huawei Technologies R&D UK Ltd. (email: David.childs@huawei.com)

Paul Harvey is with School of Computing Science, University of Glasgow, Glasgow, G12 8QQ, United Kingdom (e-mail paul.harvey@glasgow.ac.uk)

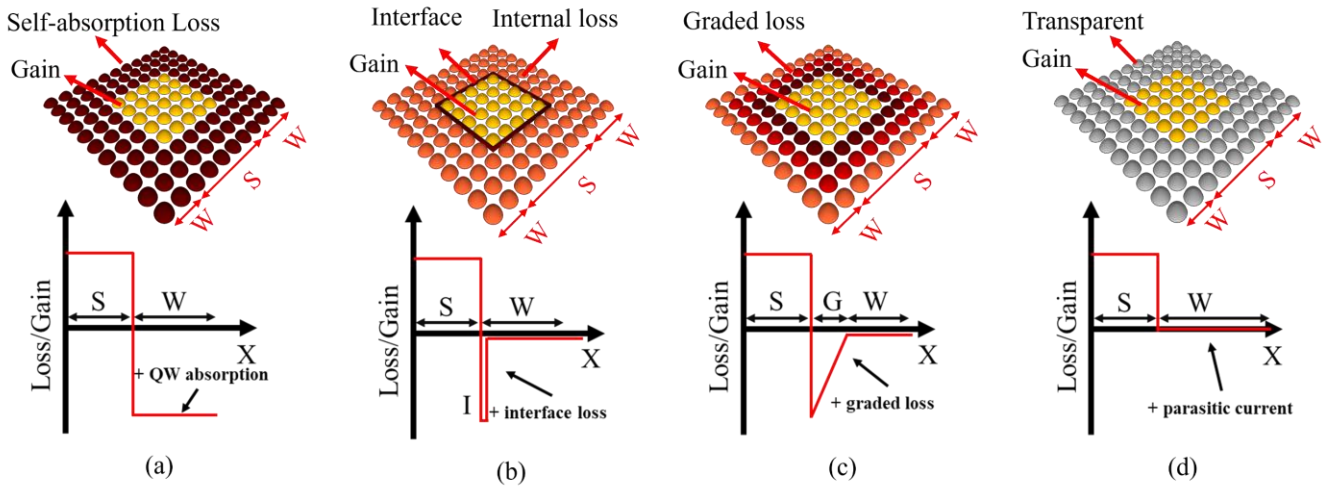

Fig. 1. Schematic and loss/gain as a function of the distance to device center of different geometry of PCSEL device, (a) absorptive boundary PCSEL; (b) butt-coupled PCSEL; (c) intermixed PCSEL; (d) dual contact PCSEL.

However, this process introduces scattering loss at the active/passive butt-coupled interface. We accommodate this in our model as an additional loss in a single PC atom thick boundary layer between gain and passive sections, as indicated in the schematic graph of loss/gain.

Figure 1(c) is PCSEL utilizing selective area quantum well intermixing (QWI). This is a solution to tune the emission/absorption wavelength by using a post-growth process to locally alter the bandgap energy of quantum well. [12] Based on this, QWI creates different sections (e.g. gain or passive) on the same wafer, and has been used to realize non-absorbing mirrors in high-power edge-emitters [13], and to locally vary the emission in broad spectral band-width devices [14]. However, this approach gives rise to a non-abrupt spatial change in the wavelength of optical transitions as it is driven by atomic diffusion. We consider a transition region (G) between the intermixed section and non-intermixed section. We assume the change in optical transition energy results in a linear variation in the QW absorption, [15-16]. The schematic graph of loss/gain characteristics of the active element indicates that the transition region, G is subject to a graded absorptive loss until enters the passive region, of width W, where light is only subject to internal loss.

We do not consider selective area epitaxy [17] as this technique, whilst reducing the gain at the lasing wavelength at the boundary, realizes a boundary with higher absorptive losses. It would therefore produce parasitic losses higher than the simple unpumped boundary in Fig 1(a).

Figure 1(d) is PCSEL with dual contacts, where the perimeter PCs are covered by another isolated contact (C2), providing the ability to independently control the current to the active element in the boundary PC region. We consider the boundary to be transparent, with no internal loss in the perimeter region. Our simulation does not generate spontaneous emissions in the boundary region. The schematic graph illustrates the loss/gain characteristics of the active element in this case. Multiple contact laser devices typically utilize shallow etching of the contact and waveguide layers [18-19] and have been employed in mode-locked edge emitting lasers [20] and PCSELs [21].

III. Probabilistic Markov Chain Model

The probabilistic Markov chain (PMC) model links the microscopic coupling coefficients (κ) and the macroscopic device-level loss (α) of the PCSEL device using a Markov chain logic and statistical method. [22] The PMC model does not perform any solutions to Maxwell's equations, rather it relies upon the input of scattering coefficient that can be determined experimentally [23-24], or from simulation. [25-28] With those parameters (in cm^{-1}), the probabilities of light scattering to different cardinal directions, out of plane, and to internal loss are then calculated. At each PC atom, for each time-step the input light is redistributed to different directions based on these probabilities. If the PC is on the edge of the PC area, exiting optical power is collected and contributes to the total in-plane loss, being the sum of the in-plane loss of all edge PC atoms. The internal loss and out-of-plane loss are also summed at each PC atom. We can use the out-of-plane loss to generate a near-field pattern of the simulated device. The simulation is terminated at a time step where we consider the simulation to have converged. This is determined by completing a few simulations with very long runtimes and choosing a suitable timestep where the in-plane loss is within 0.1 cm^{-1} of this "infinite" case [29].

Figure 2(a) shows schematic of a simple PCSEL (not including the unpumped boundary discussed in detail later) and the PC atom-to-atom optical power scattering at play. This schematic captures the essence of the PMC model, where optical power in each of the cardinal directions of the PC is generated and scattered between PC atoms. Input PC scattering coefficients apply to each PC element, with in-plane loss being calculated at the edge of PC region. Internal loss and radiative loss are also considered at each PC atom, and can be summed once convergence is achieved. [30] This allows the device level losses to be calculated for different sizes and shapes of PCSEL, and different scattering parameters of the PC.

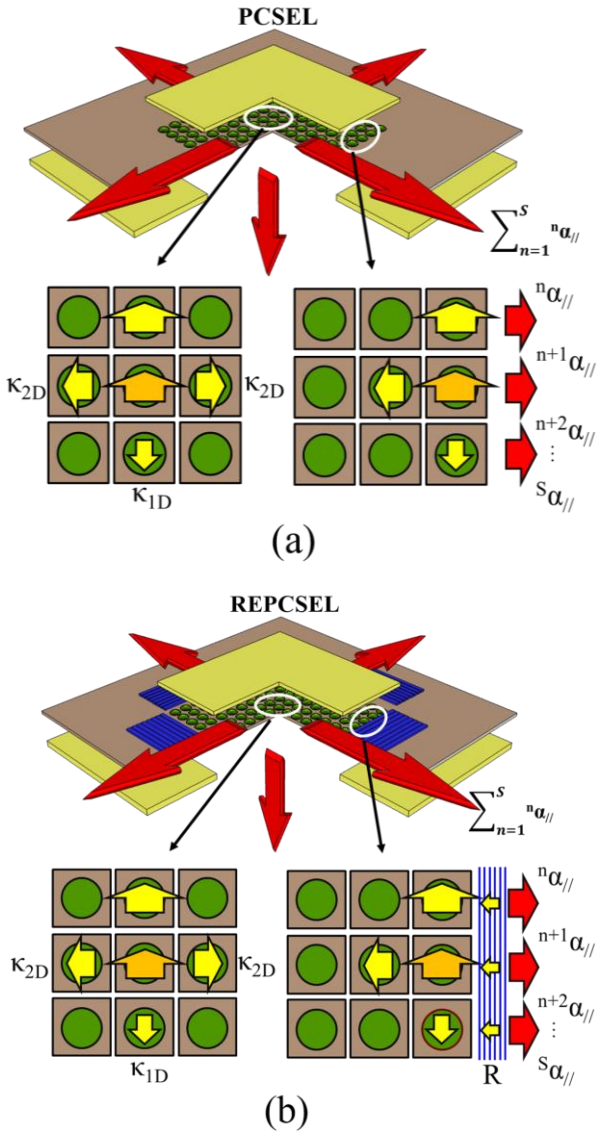

Fig. 2. Schematic, the definition of in-plane coupling coefficients (κ_{1D} & κ_{2D}) and algorithm of calculating in-plane loss in PMC model of (a) PCSEL; (b) REPCSEL.

The PMC method allows the effectiveness of changing the PCSEL perimeter to be readily and rapidly simulated. Figure 2(b) shows the schematic of a resonator embedded PCSEL (REPCSEL). [31] Here the photonic crystal region is surrounded by a 1st order DBR mirror on each edge. In the PMC model, the in-plane DBR is represented as a mirror with power reflectivity to the lasing mode that can be arbitrarily changed with R = 0 being the simple PCSEL in Figure 2(a).

Figure 3(a) shows the power-current (L-I) curve of an InP-based PCSEL (black line with dots). The PCSEL has 0.4 um period with a side of 400 um (1000 #PC) operating at 1295 nm. The L-I of a REPCSEL, nominally identical to the PCSEL, but with 100 periods of DBR surrounding the PC I also plotted. We previously reported results from devices with a side of 200 um. [31]. It can be seen from figure 3(a) that the threshold current (green dots) for REPCSEL is 730 mA of PCSEL is 880 mA. The slope efficiency, η_{SE}, is also extracted (green dotted lines), where the REPCSEL has η_{SE} = 14.1 mWA^{-1}, PCSEL with η_{SE} = 3.4 mWA^{-1}. The calculated threshold current density of REPCSEL and PCSEL is 421 Acm^{-2} and 569 Acm^{-2}. As previously reported, [31] the coupling coefficients of the PCSEL and REPCSEL are κ_{1D} = 113.2 cm^{-1}, κ_{2D} = 2.4 cm^{-1}, $\alpha_{\perp}$ = 1 cm^{-1}, α_i = 5 cm^{-1} which can be directly used as the input parameters of the PMC model. Using the PMC model with these input parameters, the in-plane loss of REPCSEL and PCSEL are determined to be 5.5 cm^{-1} and 39.6 cm^{-1}, respectively.

Figure 3(b) plots the current density-gain (J-G) characteristics of the active material used in this PCSEL/REPCSEL. This was obtained by length dependent characterization of broad area lasers. Fitting of the J-G characteristics of the active element (green dotted line) was made using:

$$J_{th} = J_0 exp(g_{th}/g_0) \quad (1)$$

Where J_{th} is threshold current density, J_0 is transparent current density, g_{th} is threshold gain, g_0 is a differential gain coefficient. This yielded J_0 = 380 Acm^{-2} and g_0 = 120 cm^{-1}.

We now use the following equation for η_{SE} to continue the fitting [7]:

$$\eta_{SE} = \frac{1.24}{\lambda}(1-A)\eta_i \frac{\frac{1}{2}\left(1+2\sqrt{R}\cos\theta+R\right)\alpha_{\perp}}{\left(1+\sqrt{R}\cos\theta\right)\alpha_{\perp}+\alpha_{//}+\alpha_i} \quad (2)$$

Where λ is the lasing wavelength, in this case, 1.295 um. A is an absorption constant, defining the ratio of the power absorbed in the substrate to the total output power, which is assumed to be 0.1. η_i is the internal quantum efficiency of the quantum well, which was measured to be 0.5. R is the reflectivity of the vertical mirror, which in this case R represents the reflectivity of the p-contact and is estimated to be 0.4 [5]. With the parameters above, the aforementioned PMC simulated values for $\alpha_{//}$ we use a single fit parameter of the radiative rate (5.0 cm^{-1}). The calculated slope efficiency of REPCSEL and PCSEL are 14.2 mWA^{-1} and 3.4 mWA^{-1}, and the threshold gain values are 11.8 cm^{-1} and 44.9 cm^{-1}, respectively. These points are plotted in green (slope and threshold) in Figures 3(a) and 3(b). A very good agreement with experimental results is obtained in both cases.

IV. Simulation Input and Output

We now discuss the input parameters we use in the simulation of our proposed device structures to explore routes to maximize PCE. Table 1 presents input parameters we used that are mainly from an InP-based PCSEL from literature [32]. λ here is the emitted wavelength of the operating device, while lattice constant a, is 480 nm which represents the wavelength of light in PC layer. The size of device, S is represented the diameter of p-electrode, in this case S = ϕ200um. κ_{1D} represent the 180° in-plane coupling strength, while κ_{2D} represent the 90° in-plane coupling strengths. The difference between κ_{2D+} and κ_{2D-} is caused by the asymmetry of the PC. [6-7] $\alpha_{\perp}$ and α_i are the radiation loss and internal loss.

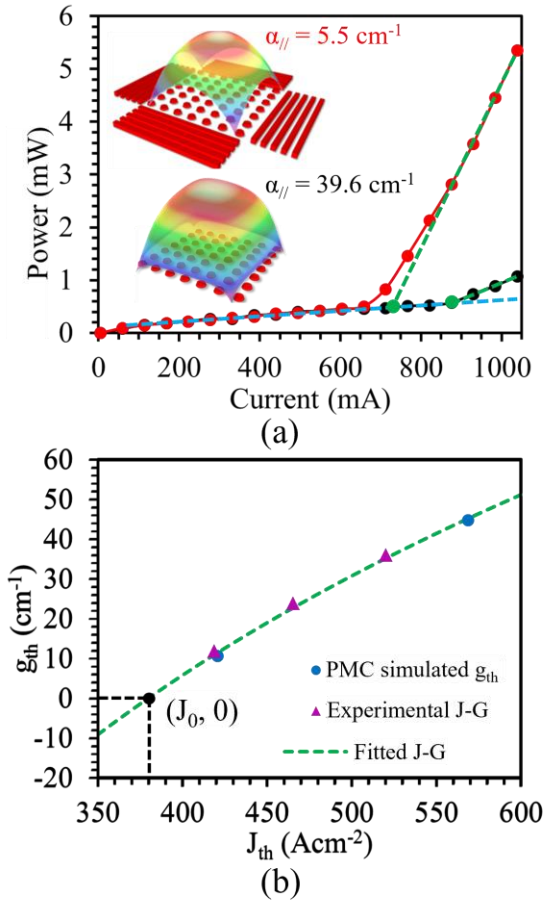

Fig. 3. (a) Measured L-I of REPCSEL (red) and PCSEL (black), dotted lines are trend line of linear region. Schematic of REPCSEL and PCSEL are insets. (b) PMC simulated (blue dots), experimental (purple dots) and fitted (green dotted line) g_{th} as a function of J_{th}.

In the absence of the authors providing J_0 and g_0 values, we use those that we obtained experimentally.

With reference to edge emitting lasers: [33]

$$\eta_d = \eta_i \frac{\alpha_m}{\alpha_m + \alpha_i} \tag{3}$$

Where η_d is a differential quantum efficiency, α_m is the mirror loss of the laser cavity. For the PCSEL, we update the definition referencing from equation 2:

$$\eta_d = \eta_i \frac{\frac{1}{2}\left(1 + 2\sqrt{R}\cos\theta + R\right)\alpha_\perp}{\left(1 + \sqrt{R}\cos\theta\right)\alpha_\perp + \alpha_{//} + \alpha_i} \tag{4}$$

Assuming the case of R = 1 and θ = 0° as:

$$\eta_d = \eta_i \frac{2\alpha_\perp}{2\alpha_\perp + \alpha_{//} + \alpha_i} \tag{5}$$

Or:

$$\eta_d = \eta_i \eta_\perp \tag{6}$$

Where:

$$\eta_\perp = \frac{2\alpha_\perp}{2\alpha_\perp + \alpha_{//} + \alpha_i} \tag{7}$$

Where $\eta_\perp$ is the PCSEL output ratio.

For this case, the gain threshold can be described as:

$$g_{th} = 2\alpha_\perp + \alpha_{//} + \alpha_i \tag{8}$$

Another output discussed below is the power conversion efficiency (PCE), defined as the total optical power output by PCSEL divided by the total electrical power input into it. [33] The equations below describe the practical approach of calculation in this paper:

$$PCE = \frac{P_{out}}{P_{in}} = \frac{P_{chosen}}{I_{in}V_{in}} \tag{9}$$

Where the chosen power, P_{chosen} is 1 W; V_{in} is based on typical I-V characteristics from the literature [32]:

$$V = V_0 + IR \tag{10}$$

Where V_0 = 0.82 V and R = 0.18 Ω. I_{in} is based on the calculated η_{SE} by the PMC model:

$$\eta_{SE} = \frac{P_1 - P_2}{I_1 - I_2} \tag{11}$$

Where P_1 is the chosen power 1 W, P_2 is the power at threshold current, which is almost 0 as reported in literature [32], I_1 is the input current I_{in}, I_2 is the threshold current Ith, then we have:

$$I_{in} = \frac{1}{\eta_{SE}} + I_{th} \tag{12}$$

We note that a key requirement for PCE improvement in the PCSEL is the development of technologies that increase the vertical mirror reflectivity R, without impacting the electrical characteristics. Furthermore, all parasitic losses should be minimized, and radiative loss "right-sized" to ensure high η_d and low g_{th}. Our work focusses on device designs that address this later requirement. We point out in the results below that we use state-of-the-art input parameters at the time of writing. Expected future improvements in vertical mirror technology, increasing R towards 1, will significantly increase the PCE values obtained.

TABLE I
INPUT PARAMETERS FOR PMC MODEL AND DATA PROCESSING

Wavelength (λ)	1550 nm	**κ_{2D+}**	197 cm^{-1}
Lattice constant (a)	480 nm	**κ_{2D-}**	176 cm^{-1}
Size (S)	Φ200 um	**$\alpha_\perp$**	8 cm^{-1}
Vertical reflectivity (R)	0.4	**α_i**	9 cm^{-1}
Interference phase (θ)	0°	**J_0**	380 Acm^{-2}
κ_{1D}	468 cm^{-1}	**g_0**	120 cm^{-1}

V. ABSORPTIVE PC BOUNDARY

Figure 4(a) shows a schematic of the absorptive boundary PCSEL. Initially, the size of the contact (yellow dots) is fixed at S = 420 #PC, and the width of boundary region W (dark red dots) varies from 50 to 450 #PC. Lasing occurs in the contacted region, S, and self-absorption (κ_{ab}) is considered for the unpumped boundary of width W. This absorption coefficient (κ_{ab}) is dictated by the MQW design and detuning between active element peak gain and the PCSEL lasing wavelength. In this work we estimate κ_{ab} = 100 cm^{-1}. [7] We apply this κ_{ab} to

the boundary area, contributing to the device level internal loss.

Figure 4(b) plots the calculated in-plane loss (black dots) and internal loss (red dots) as a function of W. As expected, the in-plane loss, $\alpha_{//}$, reduces to zero as W is increased, but due to self-absorption, the device level internal loss α_i increases. This interdependence has been previously reported [8]. The in-plane loss reduces to essentially zero (< 0.1 cm^{-1}) for W > 350 #PC, this improvement comes with an increase of α_i from 9 to ~31 cm^{-1}.

Having determined the losses, we move on to the total parasitic losses and output ratio. Figure 4(c) plots the total parasitic loss ($\alpha_{parasitic} = \alpha_{//}+\alpha_i$) and calculated output ratio ($\eta_\perp$) as a function of W for the absorptive boundary PCSEL. Total parasitic loss reduces from 87 cm^{-1} (W = 0), asymptotically reaching a value of 31 cm^{-1} at W > 350 #PC. This leads to $\eta_\perp$ increasing from 0.08 (W = 0) to 0.2 (W > 350 #PC).

So, for the absorptive boundary PCSEL with input parameters mentioned above, W = 350 #PC is needed to minimize the parasitic loss (or zero the in-plane loss). Then for case W = 350 #PC, the effect of size, S is explored. Figure 4(d) plots the total parasitic loss, $\alpha_{parasitic}$ and calculated output ratio, $\eta_\perp$ as a function of S for the absorptive boundary PCSEL. $\alpha_{parasitic}$ reduces from 79 (S = 100 #PC) to 17 cm^{-1} (S = 1000 #PC). And this reduction leads to $\eta_\perp$ increasing from 0.09 to 0.31.

Then the effect of S on threshold current, I_{th} and power conversion efficiency, PCE is explored. Figure 4(d) plots I_{th} and PCE as a function of S. I_{th} increases from ~0.02 to 1.09 A. While PCE increases from 0.03 (S = 100 #PC) and reaches a maximum value of 0.12 at S = ~850 #PC.

This result highlights that this approach to improving PCE is effective, but the efficacy is limited due to the high internal loss of the absorptive boundary region. For ease of comparison, the results presented in this section are denoted by solid lines in the following figures (Figures 5-7). Reducing the QW number to reduce absorption requires the reduction in total device loss to be a valid approach [7, 35]. Detuning the gain peak is an additional route to reducing self-absorption [36], but this again comes with a reduction in operating characteristics and increased temperature sensitivity.

VI. BUTT-COUPLED ACTIVE/PASSIVE PCSEL

Figure 5(a) plots the schematic of the PCSEL with a butt-coupled passive PC containing boundary region. A scattering interface (dark red line) separates the passive region from gain region (this is positioned at the boundary between PC atoms in the model and has no physical size).

We initially use a value for this scattering loss of 1dB, experimentally determined for monolithically integrated edge-emitting lasers [37]. Figure 5(b) plots the total parasitic loss, $\alpha_{parasitic}$, and $\eta_\perp$ as a function of S. $\alpha_{parasitic}$ decreases from 38 to 19 cm^{-1}, with a concomitant increase of $\eta_\perp$, raising from 0.17 to 0.29. We note that total parasitic loss is very similar to those of the unpumped boundary.

Figure 5(c) plots the PCSEL threshold current, I_{th} and power conversion efficiency, PCE as a function of S. I_{th} increases from ~0.01 to 1.11 A. PCE reaches maximum at S = 700 #PC with value of 0.11. Again, higher PCE appears when S < 700 #PC.

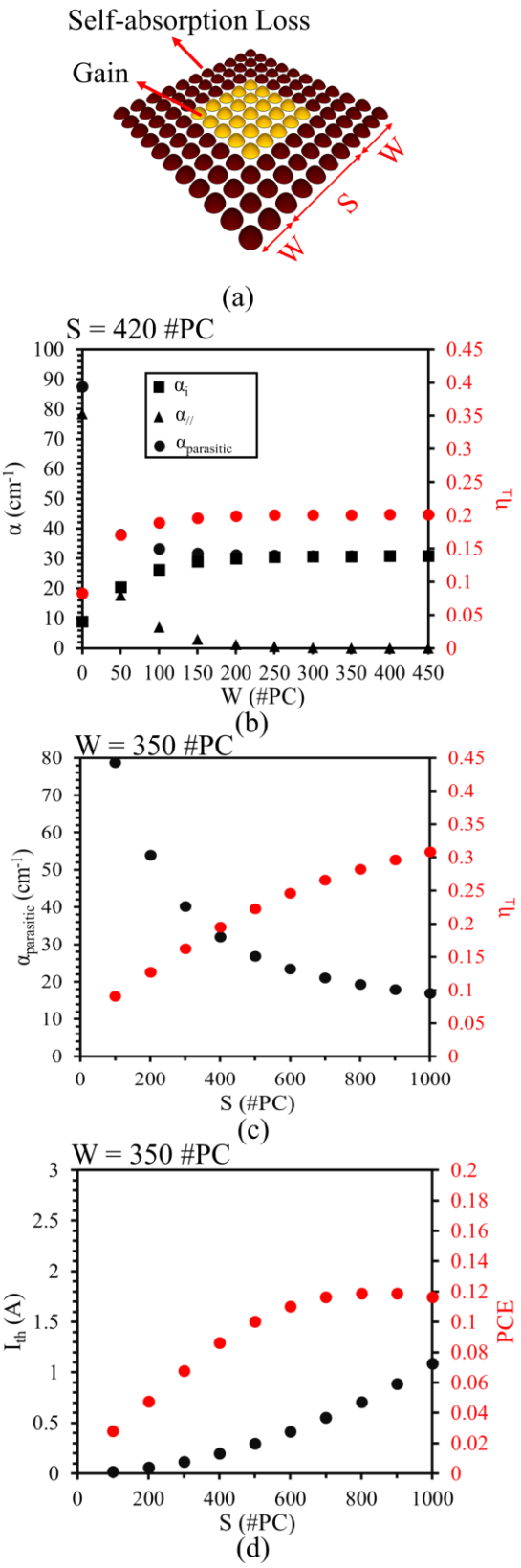

Fig. 4. (a) Schematic of absorptive boundary. Loss and output ratio as a function of (b) W and (c) S. (d)

Whilst optimal contact size is different as compared to the unpumped boundary PCSEL, the values of the threshold currents and PCE are very similar.

To further explore the effect of this interface loss on I_{th} and PCE, the effect of reducing coupling loss is simulated. Figure 5(d) plots I_{th} and PCE as a function of S with interface loss of, 0.25 dB (square dots), 0.5 dB (triangular dots) and 1 dB (circular dots). It can be seen that the I_{th} does not show significant change. As expected, the PCE increases when interface loss is reduced. For the case interface loss = 0.25 dB, PCE reaches a maximum of 0.14 at S = 500 #PC; the case interface loss = 0.5 dB, PCE reaches a maximum of 0.13 at S = 600 #PC.

Whilst for this device the increase in PCE is not significant (other engineering choices are discussed later), by comparison to the unpumped boundary, the Butt-Coupled PCSEL allows a smaller, comparable efficiency PCSEL to be realized.

VII. Selective Area Intermixed Active/Passive PCSEL

Figure 6(a) plots a schematic of intermixed PCSEL. The gain region (yellow dots) has varied sizes, S. The intermixing technique creates a transition region, within which the wavelength shifts. In the PMC model, this transition region is assumed to have an absorption loss with linear reducing value from contact to passive boundary W. See Fig 1(d). The width of this transition region, G, is initially assumed to have a value of 50 #PC (~20um for InP based devices) [20] W and G have a total width of 350 #PC as in previous discussions.

Figure 6(b) plots the $\alpha_{parasitic}$ and $\eta_{\perp}$ as a function of S, for the case G = 50 #PC, $\alpha_{parasitic}$ shows a reduction from 33 to 15 cm^{-1}, with an increase of $\eta_{\perp}$ from 0.12 to 0.26. Figure 6(c) plots the I_{th} and PCE as a function of S. For G = 50 #PC, I_{th} shows a similar increase as butt-coupled PCSEL from ~0.02 to1.1 A. PCE reaches a maximum with value of 0.14 at S = 600 #PC.

By contrast to the intermixing of full laser structures [38-39], the thickness of semiconductor material between the surface and the MQW can be small in PCSELs, leading to the possibility for smaller transition regions. The effect of reducing the width of this transition is explored, choosing tra
-nsition thicknesses of 5 and 25 #PC, corresponding to ~2 and 10 um. Figure 6(d) plots the I_{th} and PCE as a function of S, with varied G (5, 25 and 50 #PC). I_{th} does not exhibit significant change.

For the case where G = 25 #PC, PCE has a maximum value of 0.16 at S = 600 #PC; the case G = 5 #PC, PCE has a maximum value of 0.18 at S = 500 #PC. The effect of reducing the transition thickness is to enhance the PCE and to allow the move to smaller PCSELs.

VIII. Dual Contact PCSEL

Using the characteristic boundary width W=350#PC from above, we move on to explore the effect of adding a second independent contact to the boundary layer. Figure 7(a) shows a schematic of the dual contact PCSEL; contact 1 (C1, yellow dots) has size S, and contact 2 (C2 grey dots) has fixed width W = 350 #PC. We consider a current being applied to C2 to

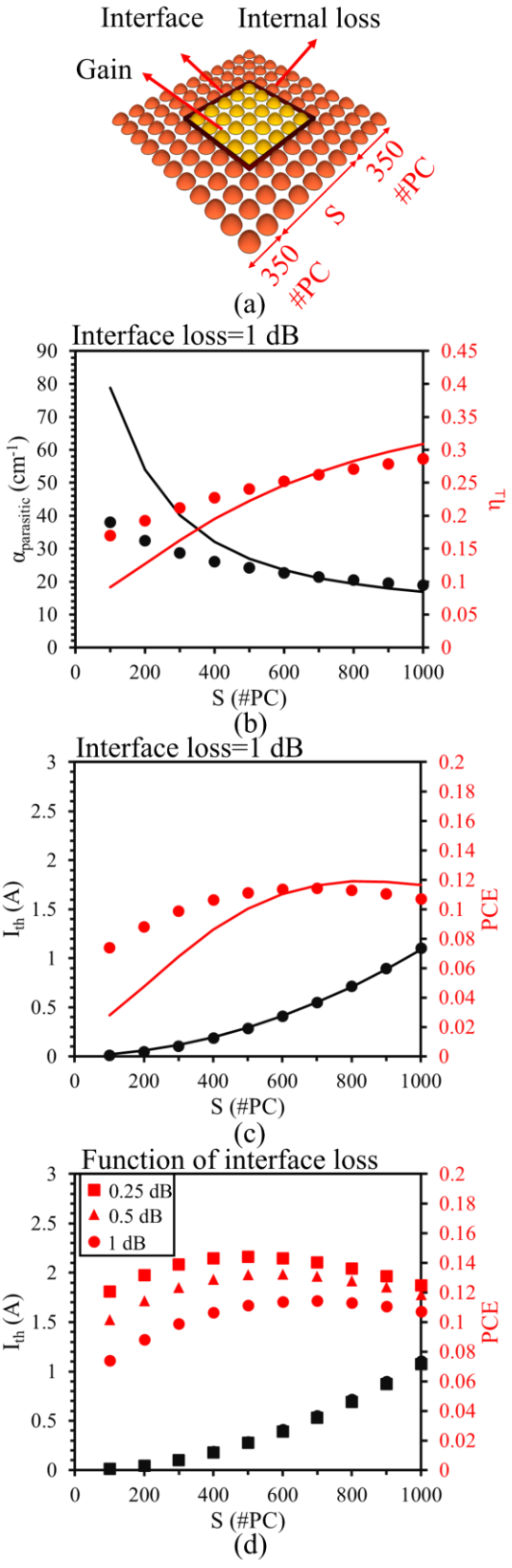

Fig. 5. (a) Schematic of butt-coupled PCSEL. (b) Parasitic loss and output ratio as a function of S. Threshold current and power conversion efficiency as a function of (c) S and (d) interface loss.

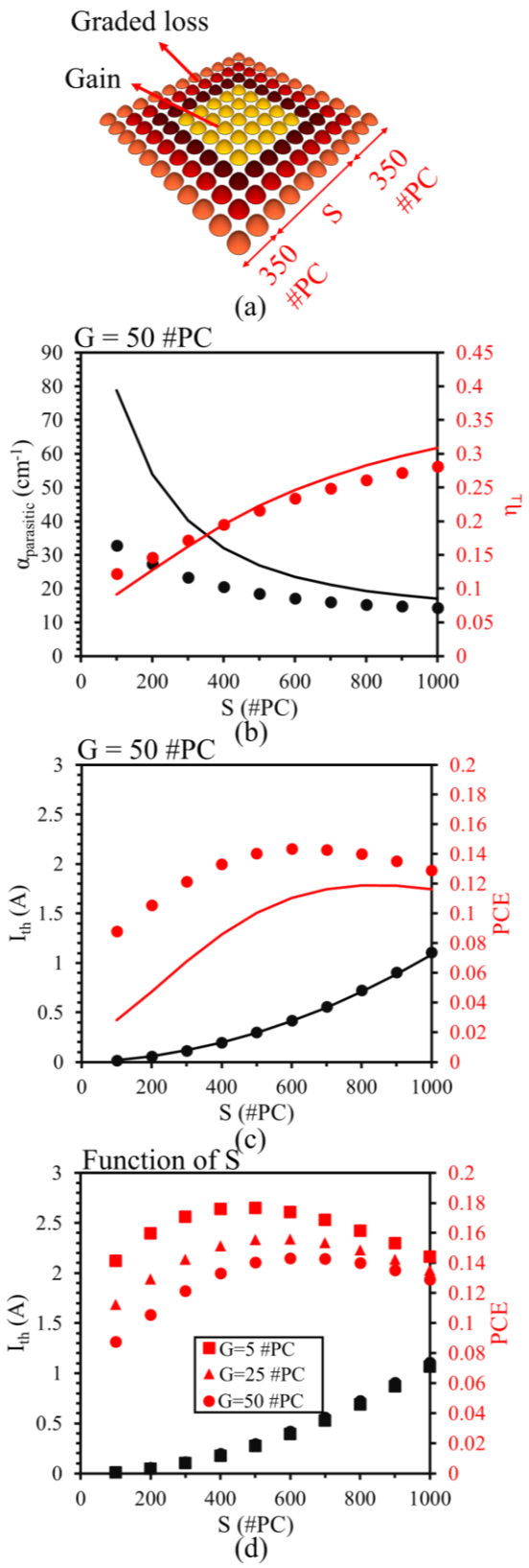

Fig. 6. (a) Schematic of intermixed PCSEL (b) Parasitic loss and output ratio as a function of S. Threshold current and power conversion efficiency as a function of (c) S and (d) G.

make the active element in the boundary PC region transparent (κ_{ab} and α_i).

The input current to the device is updated to:

$$I_{in} = I_{C1} + I_{C2} \quad (13)$$

Where I_{C1} is given by equation (12), where the threshold gain (equation 8) allows threshold current to be determined from the assumed values of J_0 and g_0. The slope efficiency uses the parameters in table 1 and the calculated parasitic losses to determine $\eta_\perp$. The transparent current (I_{C2}) is calculated from J_0 and the size of C2:

$$I_{C2} = J_0 S_{C2} \quad (14)$$

Figure 7(b) plots the total parasitic loss, $\alpha_{parasitic}$, and $\eta_\perp$ as a function of S. The parasitic loss shows a gradual reduction as the size of contact 1 is increased, reducing from 13 to 11 cm^{-1}. The output ratio shows an increase with increasing contact 1 size, rising from 0.36 to 0.43. In the case of an infinitely thick boundary PC layer, it is reasonable to expect these figures to remain constant. Their small variation is attributed to their finite size.

Figure 7(c) plots the PCSEL threshold current, I_{th} and power conversion efficiency, PCE as a function of contact 1 size. I_{th} shows an increase from 0.6 to 2.7 A as S increases from 100 to 1000 #PC. This increase in threshold current is mainly a function of the area scaling (of both C1 and C2) as losses remain almost constant. The PCE shows a significant increase compared to the absorptive boundary case (Fig. 4(d)). This is notwithstanding the additional current required to make the boundary transparent. The PCE has a maximum value of ~0.19 (0.190) at S = 200 #PC.

We then continue to explore the effect of the contact 2 size to I_{th} and PCE for the case with highest PCE, S = 200 #PC. Figure 7(d) plots the I_{th} and PCE as a function of the width of contact 2, W. I_{th} shows an increase from 0.1 to 4.2 A. PCE has a maximum value of ~0.19 (0.193).

IX. DISCUSSION

For PCSELs in general, improvement in vertical mirror technologies, reduction of parasitic losses, and right-sizing radiative loss are required. The current approach to PCE enhancement by using an absorptive boundary leads to an effective zeroing of in-plane loss, but an enhancement in internal loss. To engineer such devices, reducing the number of QWs in the active region will result in lower absorption and hence higher PCE. However, this can only be achieved by reducing all losses (radiative and parasitic) to reduce threshold gain. There is also design room for detuning, but this impacts threshold current.

In order to engineer Butt-coupled PCSELs, the interface scattering and internal loss of the PC boundary layer (not discussed here) need reducing. A drive to smaller PCSELs breaks the need for PC shapes that have lower coupling to enable spatial spectral mode control for large areas [6]. The increase of the PC scattering strength will in turn reduce parasitic at the butt-joint, in turn driving up PCE.

The intermixing approach shows promise. The use of intermixing very close to the MQW active, followed by PC

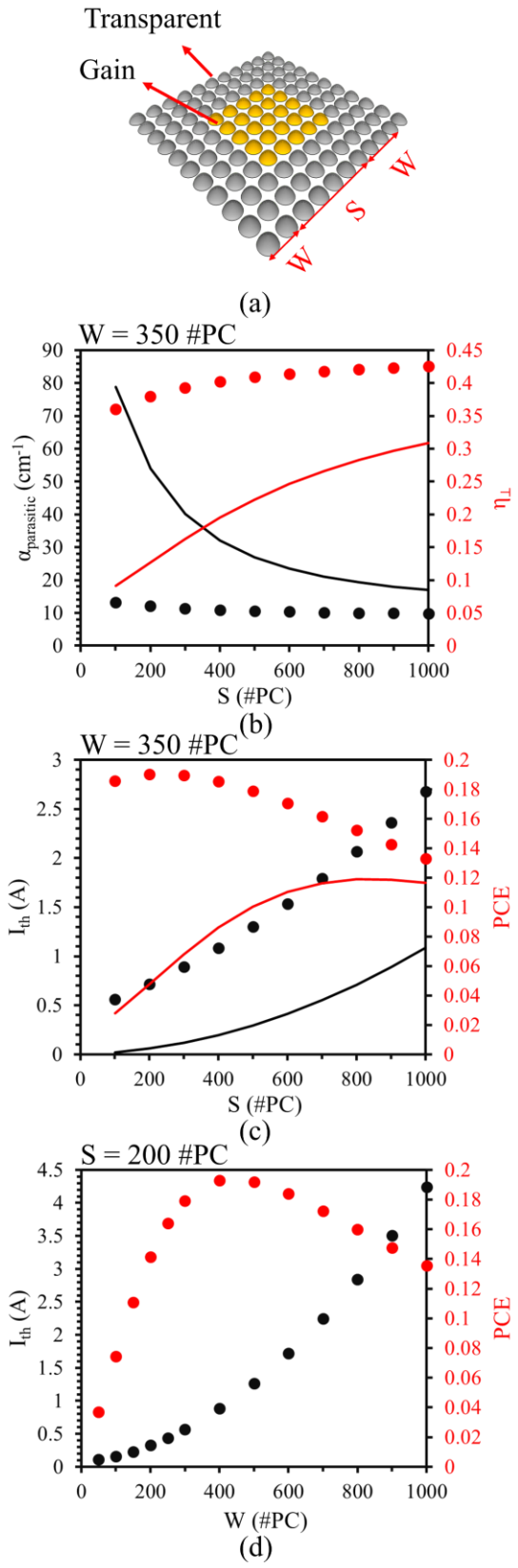

Fig. 7. (a) Schematic of dual contact. (b) Parasitic loss and output ratio as a function of S. Threshold current and power conversion efficiency as a function of (c) S and (d) W.

definition and epitaxial re-growth may provide a route to higher PCE without the need for additional drive electronics. The minimization of the graded transition region thickness is therefore an interesting route to pursue. The relative technological ease of realizing a low scattering butt-joint, or thin intermixed transition region may decide the best approach. However, the butt-joint does offer the opportunity to create undoped passive waveguides, adding a possible advantage of reduced internal loss in the passive element.

The Dual Contact approach benefits over all other approaches by zeroing parasitic loss in the boundary. However, this occurs at a price: the additional current supplied to the boundary (and associated heat, and energy required to remove that heat). This would again be reduced in the case of fewer QWs, reducing the C2 current as transparency current density is lower. Again, a push to lower PCSEL size allows higher coupling strength PCs, further reducing the in-plane loss, reducing the required PC boundary size, and additional current.

X. SUMMARY

A range of device designs to minimize parasitic loss in PCSELs have been explored using the Probabilistic Markov chain (PMC) model. We described the inputs and outputs to the simulation and described the effects of butt-coupled passive sections in the boundary PC region, selective area intermixing the active element in the boundary PC region, and using a second contact to the boundary PC. The additional contact device renders the boundary transparent, whilst the other two approaches maintain an internal loss only.

Various characteristics of these techniques were explored and the PCE for an exemplary 1 W source were discussed. For the butt-coupled device we considered improvement in the fabrication technologies leading to reduced scattering loss at the etched/regrown waveguide interface. For the selective area intermixed device, a reduction in the lateral extent of the transition from active to passive wavelengths is also considered. In the case of the dual contact device, the highest PCE was shown to be possible, given the input parameters taken from the literature. A critical comparison of the approaches was made, and possible future research avenues discussed.

REFERENCES

[1] S. Noda, M. Yoshida, T. Inoue *et al.,* "Photonic-crystal surface-emitting lasers," *Nat. Rev. Electr. Eng*., vol. 1, pp. 802–814, 2024, doi: 10.1038/s44287-024-00113-x.

[2] S. Noda, T. Inoue, M. Yoshida, J. Gelleta, M. De Zoysa, and K. Ishizaki, "High-power and high-beam-quality photonic-crystal surface-emitting lasers: a tutorial," *Adv. Opt. Photon*., vol. 15, no. 4, pp. 977-1032, 2023, doi: 10.1364/AOP.502863.

[3] M. Yoshida, S. Katsuno, T. Inoue *et al.,* "High-brightness scalable continuous-wave single-mode photonic-crystal laser," *Nature*, vol. 618, pp. 727–732, 2023, doi: 10.1038/s41586-023-06059-8.

[4] K. Hirose, Y. Liang, Y. Kurosaka *et al.,* "Watt-class high-power, high-beam-quality photonic-crystal lasers," *Nature Photon*., vol. 8, pp. 406–411, 2014, doi: 10.1038/nphoton.2014.75.

[5] K. Emoto, T. Koizumi, M. Hirose *et al.,* "Wide-bandgap GaN-based watt-class photonic-crystal lasers," *Commun. Mater*., vol. 3, p. 72, 2022.

[6] M. Yoshida, M. De Zoysa, K. Ishizaki *et al.,* "Double-lattice photonic-crystal resonators enabling high-brightness semiconductor lasers with symmetric narrow-divergence beams," *Nature Mater*., vol. 18, pp. 121–128, 2019, doi: 10.1038/s41563-018-0242-y.

[7] M. Yoshida, M. De Zoysa, K. Ishizaki *et al.,* "Double-lattice photonic-crystal resonators enabling high-brightness semiconductor lasers with symmetric narrow-divergence beams," *J. Phys. Photonics*, vol. 3, no. 2, 2021, Art. no. 022006, doi: 10.1088/2515-7647/abea06.

[8] J. Liu, X. Zhao, Z. Bian *et al.,* "Interdependence of parasitic losses in photonic crystal surface emitting lasers," *AIP Advances*, vol. 15, no. 4, 2025, Art. no. 045321, doi: 10.1063/5.0252646.

[9] M. Nishimoto, K. Ishizaki, K. Maekawa, K. Kitamura and S. Noda, "Photonic-crystal surface-emitting laser," *Appl. Phys. Express*, vol. 6, no. 4, 2013, Art. no. 042002, doi: 10.7567/APEX.6.042002.

[10] Y. Kurosaka, S. Iwahashi, Y. Liang *et al.,* "On-chip beam-steering photonic-crystal lasers," *Nature Photon*., vol. 4, pp. 447–450, 2010, doi: 10.1038/nphoton.2010.118.

[11] H. Matsubara, S. Yoshimoto, H. Saito *et al.,* "GaN photonic-crystal surface-emitting laser at blue-violet wavelengths," *Science*, vol. 319, no. 5862, pp. 445–447, 2008.

[12] J. H. Marsh, "Quantum well intermixing for optoelectronics," *Semicond. Sci. Technol*., vol. 8, no. 6, p. 1136, 1993.

[13] L. Hou, R. Dylewicz, M. Haji, P. Stolarz, B. Qiu and A. C. Bryce, "Monolithic 40-GHz Passively Mode-Locked AlGaInAs–InP 1.55-μ m MQW Laser With Surface-Etched Distributed Bragg Reflector," *IEEE Photon. Technol. Lett.*, vol. 22, no. 20, pp. 1503-1505, Oct.15, 2010, doi: 10.1109/LPT.2010.2064764.

[14] K. J. Zhou et al., "Quantum dot selective area intermixing for broadband light sources," *Optics Express*, vol. 20, no. 24, pp. 26950-26957, Nov. 2012. doi: 10.1364/OE.20.026950.

[15] T. Tabbakh, "Diffusion and Quantum Well Intermixing," in *Recent Advances in Nanophotonics - Fundamentals and Applications, IntechOpen*, 2020. doi: 10.5772/intechopen.92440.

[16] A. S. Helmy, A. C. Bryce, D. C. Hutchings, J. S. Aitchison, and J. H. Marsh, "Band gap gratings using quantum well intermixing for quasi-phase-matching," *J. Appl. Phys*., vol. 100, no. 12, 2006, Art. no. 123107, doi: 10.1063/1.2402034.

[17] X. Zhao, A. F. McKenzie, C. W. Munro *et al.,* "Large-area 2D selective area growth for photonic crystal surface emitting lasers," *J. Cryst. Growth*, vol. 603, 2023, Art. no. 127036, doi: 10.1016/j.jcrysgro.2022.127036.

[18] L. A. Coldren, G. A. Fish, Y. Akulova *et al.,* "Tunable semiconductor lasers: a tutorial," *J. Lightw. Technol.*, vol. 22, no. 1, pp. 193-202, Jan. 2004, doi: 10.1109/JLT.2003.822207.

[19] M. A. Tran, D. Huang, and J. E. Bowers, "Tutorial on narrow linewidth tunable semiconductor lasers using Si/III-V heterogeneous integration," *APL Photonics*, vol. 4, no. 11, 2019, Art. no. 111101, doi: 10.1063/1.5124254.

[20] H. A. Haus, "Mode-locking of lasers," *IEEE J. Sel. Topics Quantum Electron*., vol. 6, no. 6, pp. 1173-1185, Nov.-Dec. 2000, doi: 10.1109/2944.902165.

[21] R. Taylor, D. Childs, P. Ivanov *et al.,* "Electronic control of coherence in a two-dimensional array of photonic crystal surface emitting lasers," *Sci. Rep*., vol. 5, 2015, Art. no. 13203, doi: 10.1038/srep13203.

[22] J. Liu, Y. Gao, P. Ivanov, P. Harvey, and R. Hogg, "Probabilistic Markov chain modeling of photonic crystal surface emitting lasers," *Appl. Phys. Lett.*, vol. 123, no. 26, 2023, Art. no. 261107, doi: 10.1063/5.0168073.

[23] K. Sakai, E. Miyai, and S. Noda, "Coupled-wave model for square-lattice two-dimensional photonic crystal with transverse-electric-like mode," *Appl. Phys. Lett*., vol. 89, no. 2, 2006, Art. no. 021101, doi: 10.1063/1.2220057.

[24] T. Inoue, T. Kim, S. Katsuno *et al.,* "Measurement and numerical analysis of intrinsic spectral linewidths of photonic-crystal surface-emitting lasers," *Appl. Phys. Lett*., vol. 122, no. 5, 2023, Art. no. 051101, doi: 10.1063/5.0135042.

[25] Y. Liang, C. Peng, K. Ishizaki *et al.,* "Three-dimensional coupled-wave analysis for triangular-lattice photonic-crystal surface-emitting lasers with transverse-electric polarization," *Opt. Express*, vol. 21, no. 1, pp. 565–580, 2013, doi: 10.1364/OE.21.000565.

[26] Y. Liang, C. Peng, K. Sakai, S. Iwahashi, and S. Noda, "Three-dimensional coupled-wave analysis for square-lattice photonic crystal surface emitting lasers with transverse-electric polarization: finite-size effects," *Opt. Express*, vol. 20, no. 14, pp. 15945–15961, 2012, doi: 10.1364/OE.20.015945.

[27] Y. Yang, C. Peng, Y. Liang, Z. Li, and S. Noda, "Three-dimensional coupled wave theory for the guided mode resonance in photonic crystal slabs: TM-like polarization," *Opt. Lett*., vol. 39, no. 15, pp. 4498–4501, 2014, doi: 10.1364/OL.39.004498.

[28] T. Inoue, R. Morita, M. Yoshida, M. De Zoysa, Y. Tanaka, and S. Noda, "Comprehensive analysis of photonic-crystal surface-emitting lasers via time-dependent three-dimensional coupled-wave theory," *Phys. Rev. B*, vol. 99, no. 3, 2019, Art. no. 035308, doi: 10.1103/PhysRevB.99.035308.

[29] J. Liu, D. Kim, Z. Bian, J. Feng, Y. Gao, P. Harvey, and R. Hogg, "Convergence criteria for probabilistic Markov chains modelling of photonic crystal surface emitting lasers," in *Proc. SPIE 12440, Novel In-Plane Semiconductor Lasers XXII*, 2023, p. 124400D. doi: 10.1117/12.2649077.

[30] J. Liu, X. Zhao, Z. Bian, S. J. Sweeney, and R. Hogg, "Optimization of pumping geometry of photonic crystal surface emitting lasers," in *Proc. SPIE Physics and Simulation of Optoelectronic Devices XXXIII*, vol. 13360, 2025, Art. no. 1336004, doi: 10.1117/12.3042883.

[31] Z. Bian, X. Zhao, J. Liu *et al.,* "Resonator embedded photonic crystal surface emitting lasers," *npj Nanophoton*., vol. 1, p. 13, 2024, doi: 10.1038/s44310-024-00014-9.

[32] T. Aoki, Y. Itoh, K. Fujii *et al.,* "High-power high-beam-quality 1550-nm-wavelength InP-based photonic-crystal surface-emitting laser," in *Proc. SPIE Novel In-Plane Semiconductor Lasers XXIV*, vol. PC13385, 2025, Art. no. PC133850Y, doi: 10.1117/12.3037797.

[33] L. A. Coldren, S. W. Corzine, and M. L. Mašanović, "Mirrors and Resonators for Diode Lasers," in *Diode Lasers and Photonic Integrated Circuits*, 2nd ed. Hoboken, NJ, USA: Wiley, 2012, ch. 3, pp. 91–155.

[34] L. A. Coldren, S. W. Corzine, and M. L. Mašanović, "A Phenomenological Approach to Diode Lasers," in *Diode Lasers and Photonic Integrated Circuits*, 2nd ed. Hoboken, NJ, USA: Wiley, 2012, ch. 2, pp. 45–90.

[35] P. M. Ilroy, A. Kurobe, and Y. Uematsu, "Analysis and application of theoretical gain curves to the design of multi-quantum-well lasers," *IEEE J. Quantum Electron.*, vol. 21, no. 12, pp. 1958–1963, Dec. 1985, doi: 10.1109/JQE.1985.1072606.

[36] A. Ramdane, F. Devaux, N. Souli, D. Delprat and A. Ougazzaden, "Monolithic integration of multiple-quantum-well lasers and modulators for high-speed transmission," in *IEEE Journal of Selected Topics in Quantum Electronics*, vol. 2, no. 2, pp. 326-335, June 1996, doi: 10.1109/2944.577388.

[37] Y. Cheng, J. Pan, S. Liang, W. Feng, Z. Liao, F. Zhou, B. Wang, L. Zhao, H. Zhu, and W. Wang, "Butt-coupled MOVPE growth for high-performance electro-absorption modulator integrated with a DFB laser," *J. Crystal Growth*, vol. 308, no. 2, pp. 297–301, 2007, doi: 10.1016/j.jcrysgro.2007.09.004.

[38] L. Hou, M. Haji, J. Akbar, J. H. Marsh, and A. C. Bryce, "AlGaInAs/InP monolithically integrated DFB laser array," *IEEE J. Quantum Electron.*, vol. 48, no. 2, pp. 137–143, Feb. 2012, doi: 10.1109/JQE.2011.2174455.

[39] J. H. Marsh, "Quantum well intermixing revolutionizes high power laser diodes," *Laser Technik J.*, vol. 4, no. 6, pp. 32–35, 2007, doi: 10.1002/latj.200790190.

Jingzhao Liu received the B.E. degree, from China University of Geoscience (Beijing) in Measurement and Control Technology and Instrumentation in 2018, M. Sc degree from University of Glasgow in electronics and electrical engineering in 2020. He is expecting his Ph.D. degree in December 2025.

During his M.Sc. and Ph.D. study, he focused on the photonic crystal surface emitting lasers (PCSELs). From October to December in 2023 he was a visiting researcher in National Institute of Information and Communications Technology (NICT), Tokyo, Japan.

Xingyu Zhao received the B.E. degree from Central South University of Forestry and Technology and Bangor University in Electronic Information Engineering in 2018, M. Sc degree from University of Glasgow in electronics and electrical engineering in 2019. He is expecting his Ph.D. degree in January 2026. During his Ph.D. study, he focused on the photonic crystal surface emitting lasers (PCSELs).

Daehyun Kim received a Ph.D. degree from Korea University. With over 10 years of experience in III-V compound semiconductor-based photonic devices and systems.

He specialized in the development of high-power photonic emitters.

Dr. Kim's work has resulted in 29 peer-reviewed paper publications and 24 registered patents—comprising 3 US patents, 12 Korean patents, and 9 PCT applications. Notably, 3 of these patents were successfully transferred for commercialization in 2024. With a strong background in academic-industrial research, Dr. Kim has consistently aimed at delivering impactful results that bridge the gap between academic and real-world applications

Jonathan R. Orchard received the M.Eng. degree in electronic engineering and the Ph.D. degree from the University of Sheffield, Sheffield, U.K., where he was involved in the design and characterization of vertical cavity lasers in 2008 and 2012, respectively. He was a Postdoctoral Researcher at the University of Sheffield where he was involved in research on various aspects of quantum dot photonic devices grown on silicon substrates, including carrier dynamics and long wavelength emission. He is currently with Vector Photonics.

David T. D. Childs, (Member, IEEE), received his Ph.D. degree from Imperial College London, London, U.K. in 2002.

He was then with the Research and Development Department of Marconi Optical Components (later Bookham and now Oclaro). Following this, he joined the Department of Electronic and Electrical Engineering, The University of Sheffield, where he was engaged in a number of projects developing semiconductor light sources from visible through to THz wavelengths. He became Lecturer with the Department of Electronic and Nanoscale Engineering, School of Engineering, University of Glasgow, Glasgow, U.K. He was then co-founder and Director of product development at Vector Photonics. He is currently Design Team Manager at Huawei Technologies R&D UK Ltd at Adastral Park, Ipswich.

Dr Childs has contributed to more than 100 journals and conference publications, and a number of patent filings.

Richard J. E. Taylor received a B.Eng., M.Sc. and Ph.D. degrees from The University of Sheffield in 2010, 2011, and 2014, respectively. and became a chartered engineer in 2020. For this work they were awarded an IET postgraduate award.

He was a JSPS Research Fellow at the University of Tokyo between 2015 and 2017, A research associate at the University of Glasgow between 2017 and 2019, a Royal Academy of Engineering enterprise fellow in 2019; and a fellow at the quantum technology enterprise centre in Bristol in 2020. Since 2020 he has been with Vector Photonics.

Dr Taylor was the recipient of the IET Sir Henry Royce Medal and the RAEng Collin Campble Mitchel award for outstanding contribution to the field of engineering.

Paul Harvey (Member, IEEE), received his M.Sci. and Ph.D. degrees in Computing Science from the University of Glasgow, U.K., in 2010 and 2015, respectively.

Formerly a JSPS Fellow, he is now a Senior Lecturer in the School of Computing Science at the University of Glasgow and Vice-Chair of the ITU-T Focus Group on AI-Native for Networks. His research focuses on autonomous systems, adaptive runtimes, and sustainable computing, with applications across network management, digital twins, and inverse design. He previously co-founded and led research at the Rakuten Mobile Innovation Studio and has contributed extensively to AI-native network standardisation. His current interests include AI-driven autonomy, digital sustainability, and the design of adaptive, evolvable systems bridging academia, industry, and global standards initiatives.

Stephen J. Sweeney (Senior Member, IEEE) received the B.Sc. (Hons.) degree in Applied Physics and the Certificate in Education from the University of Bath, UK and the Ph.D. degree in Physics from the University of Surrey, UK. His research interests include novel semiconductor materials and photonic devices. He is currently Professor of Photonics and Nanotechnology at the James Watt School of Engineering at the University of Glasgow. He holds Visiting Professorial positions at the University of Surrey, UK, the University of Wollongong, Australia, and the Ferdinand Braun Institute, Berlin, Germany. He is Chief Technology Officer for ZiNIR Ltd. (UK) and Editor of Journal of Materials Science: Materials in Electronics. Previous roles include Head of the Department of Physics at the University of Surrey, Lead Scientist for Marconi Optical Components, President of the British Science Association (Physics & Astronomy division), and Associate Editor of IEEE Journal of Quantum Electronics. He spent sabbatical leave with Arizona State University, USA, Philipps-Universität, Marburg, Germany, and was a JSPS International Invitational Fellow with the Kyoto Institute of Technology, Japan. He is a Chartered Physicist, a Fellow of The Institute of Physics and a Fellow of SPIE.

Richard A. Hogg received a BSc in Physics from The University of Nottingham, and Ph.D. degree from the University of Sheffield, Sheffield, U.K., in 1995. In 2023 he was appointed Professor of Photonics in Aston Institute of Photonic Technologies, Aston University, UK. He is Chief Technology Officer for III-V Epi Ltd. (UK), and co-founder of Vector Photonics Ltd. Previous roles include positions in industrial research and development laboratories, in the U.K. (Toshiba Cambridge) and Japan (NTT), and management roles in volume manufacturing of optical transceivers (Agilent Technologies Ipswich). He was a Senior Lecturer (2003), Reader (2007), Then Professor (2011) with the EEE Department, The University of Sheffield, Sheffield, U.K. He moved to The James Watt School of Engineering, University of Glasgow as Professor of Photonics where he served as Research Director and Head of ENE Division. He was a recipient of the RAEng Collin Campble Mitchel award for outstanding contribution to the field of engineering, and is a former JSPS Fellow and Visiting professor at The University of Kobe. His research interests include novel semiconductor photonic materials, heterostructures, and devices, spanning design, epitaxy, fabrication, and applications.